

See discussions, stats, and author profiles for this publication at: <https://www.researchgate.net/publication/263476482>

# A QM/MM Study of the Reaction Mechanism of Carboxyl Transferase Domain of Pyruvate Carboxylase from *Staphylococcus aureus*.

ARTICLE in **BIOCHEMISTRY** · JUNE 2014

Impact Factor: 3.02 · DOI: 10.1021/bi500020r · Source: PubMed

---

CITATION

1

READS

92

## 2 AUTHORS:



Xiang Sheng

Stockholm University

18 PUBLICATIONS 64 CITATIONS

[SEE PROFILE](#)



Yongjun Liu

Shandong University

87 PUBLICATIONS 513 CITATIONS

[SEE PROFILE](#)

# QM/MM Study of the Reaction Mechanism of the Carboxyl Transferase Domain of Pyruvate Carboxylase from *Staphylococcus aureus*

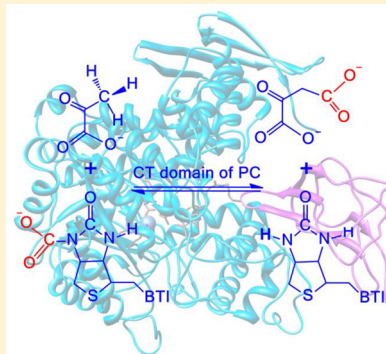
Xiang Sheng<sup>†</sup> and Yongjun Liu<sup>\*,†,‡</sup>

<sup>†</sup>School of Chemistry and Chemical Engineering, Shandong University, Jinan, Shandong 250100, China

<sup>‡</sup>Northwest Institute of Plateau Biology, Chinese Academy of Sciences, Xining, Qinghai 810001, China

 Supporting Information

**ABSTRACT:** Pyruvate carboxylase (PC) catalyzes the carboxylation of pyruvate to produce oxaloacetate. Its activity is directly related to insulin release and thus PC has recently attracted great interest as a potential target for diabetes treatment. In this article, the catalytic mechanism of the carboxyl transferase domain of PC from *Staphylococcus aureus* was investigated by using a combined quantum-mechanical/molecular-mechanical approach. Our calculation results indicate that the catalytic reaction starts from the decarboxylation of carboxybiotin to generate an enol-BTI intermediate, followed by two consecutive proton-transfer processes (from T908 to enol-BTI and from PYR to T908). During the catalytic reaction, the main-chain amide of T908 plays a key role in catching  $\text{CO}_2$  and preventing its diffusion from the active center. A triad of residues, R571, Q575, and K741, contributes both to substrate binding and enol-pyruvate stabilization. The oxyanion hole, consisting of the side-chain hydroxyl of S911 and the side-chain amino of Q870, plays an important role in stabilizing the hydroxyl anion of BTI. The coordination of the metal cation by pyruvate is a second sphere, rather than an inner sphere, interaction, and the metal cation stabilizes the species through the medium of residue K741. The decarboxylation of carboxybiotin corresponds to the highest free energy barrier of 21.7 kcal/mol. Our results may provide useful information for both the regulation of enzyme activity and the development of related biocatalytic applications.



Pyruvate carboxylase (PC, EC 6.4.1.1) is a biotin (BTI)- and MgATP-dependent multifunctional enzyme that catalyzes the carboxylation of pyruvate (PYR) to produce oxaloacetate through a two-step reaction, as shown in Scheme 1.<sup>1–5</sup> Two reaction stages take place in two physically distinct active sites. First, the tethered biotin is carboxylated through a reaction with  $\text{HCO}_3^-$  and MgATP occurring in the N-terminal biotin carboxylase (BC) domain. The formed carboxybiotin (CA-BTI) then translocates to the active site of the central carboxyl transferase (CT) domain on the neighboring polypeptide chain via the movement of the C-terminal biotin carboxyl carrier protein (BCCP) domain. Subsequently, in the CT domain, the carboxyl group transfers to PYR to generate oxaloacetate, with concomitant proton transfer from PYR to BTI.

PC is an important enzyme found in a wide range of organisms,<sup>6,7</sup> such as prokaryotes, plants, and vertebrates. In mammals, PC is crucial in various cellular anabolic processes,<sup>8–12</sup> including gluconeogenesis, lipogenesis, glyceroneogenesis, glucose-induced insulin secretion, and neurotransmitter biosynthesis, and it is relevant to tumor cell proliferation.<sup>13,14</sup> In particular, PC activity is directly related to insulin release<sup>15–18</sup> and thus has recently attracted considerable interest as a potential target for diabetes treatment.<sup>19,20</sup> PC deficiency can lead to serious diseases.<sup>21–23</sup> Therefore, a comprehensive understanding of the enzymatic mechanism of PC is meaningful and may also be of pharmacological value.

PC has two homologues that are also biotin-dependent: oxaloacetate decarboxylase (ODC), which catalyzes the transfer of an oxaloacetate carboxyl group to the membrane-bound  $\beta$ -subunit to facilitate sodium transport,<sup>24–26</sup> and transcarboxylase (TC), which catalyzes the transfer of a carboxyl moiety between two organic molecules.<sup>27</sup> These enzymes catalyze different overall reactions, but they show many obvious similarities in their active site architectures and partial reactions.<sup>28</sup> For example, the PC CT domain and TC SS subunit catalyze the exact same reaction: carboxyl group transfer from CA-BTI to substrate PYR. Thus, structural and mechanistic information for ODC and TC are also significant for the understanding of PC.

To date, several reaction mechanisms of the PC CT domain have been proposed.<sup>29–31</sup> Rétey et al. proposed a concerted mechanism in which the methyl of PYR is deprotonated by the ureido oxygen of biotin.<sup>32</sup> Stubbe et al. and Sueda et al. suggested that the reaction proceeds via a carbanion mechanism and that the deprotonation of the PYR methyl group occurs prior to the decarboxylation of CA-BTI.<sup>33–35</sup> In addition, another mechanism involving the formation of a cage

Received: January 6, 2014

Revised: June 10, 2014

Published: June 25, 2014



Scheme 1. Catalytic Reaction of PC

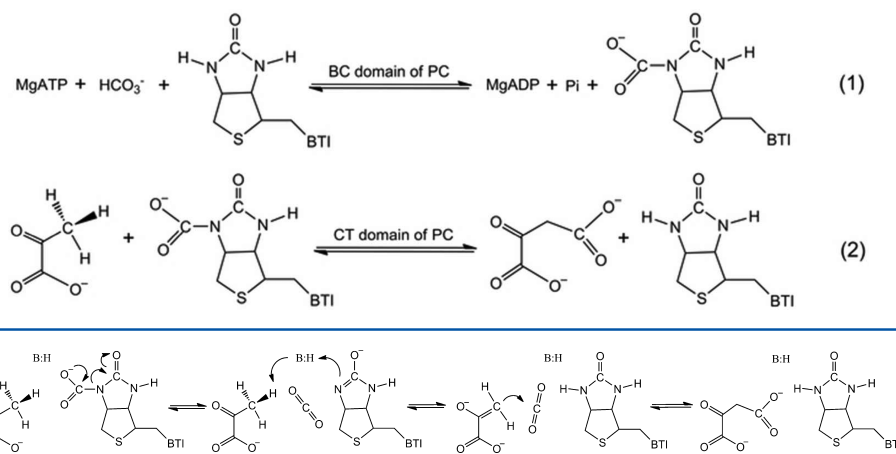


Figure 1. Proposed catalytic mechanism of CT domain of PC.

intermediate by attack of sulfur on the ureido carbon atom was also proposed.<sup>36</sup> However, according to the <sup>13</sup>C deuterium isotope effect data<sup>37,38</sup> and the structural geometries,<sup>39</sup> all of the mechanisms mentioned seem unlikely. Recently, a generally accepted mechanism has been formulated, as shown in Figure 1.<sup>40–42</sup> First, an anionic enol-BTI intermediate is formed by the decarboxylation of CA-BTI. Subsequently, a general base/acid group donates a proton to enol-BTI, which then abstracts a proton from PYR in a concerted manner to generate an enol-PYR. Finally, enol-PYR is carboxylated by the previously formed CO<sub>2</sub>. This reaction mechanism has been supported by crystal structures and mutagenesis studies.<sup>40–44</sup> In PC from *Rhizobium etli* and *Staphylococcus aureus*, mutagenesis studies revealed that a Thr residue may act as the general base/acid group and that some other residues may play important roles in the binding of PYR and CA-BTI.<sup>40–43</sup>

The complete crystal structure of PC, from *R. etli*, was first reported by St. Maurice in 2007.<sup>45</sup> Subsequently, a holoenzyme structure of PC from *S. aureus* was reported by Tong,<sup>39</sup> which is the first full-length structure binding with PYR, BTI, and metal cation. This complete structure provided significant information about the interaction between domains, the structure of the active sites, and the binding mode of substrates and cofactors. On the basis of the structural and mutagenesis studies, a domain termed the allosteric domain, or PC tetramerization (PT) domain, was suggested to be important for oligomerization and binding of the allosteric activator, acetyl-CoA.<sup>31,45</sup> *S. aureus* PC is a tetramer with a roughly cubic shape. In the active site pocket of the CT domain, the BCCP domain in the catalytic conformation was first observed, and a divalent cation that is coordinated by residues D572, H771, H773, and K741 (the residues are numbered according to their human PC equivalents) was found in the CT domain. In the active site, BTI is anchored by residues S911, K912, and T908 by hydrogen bonds. The methyl group of PYR is located 4.7 Å from the nitrogen atom of biotin, and its carbonyl group is positioned within 3.5 Å from the metal cation.

Although the CT domain of PC has been extensively explored by experiments and a rough framework of the catalytic mechanism has been sketched, a full atomistic and thermodynamic characterization still remains to be determined. For example, the detail of each elementary step is absent. Is the decarboxylation of AC-BTI concerted with the proton transfer

from the general base/acid group to BTI? If this decarboxylation step occurs alone, then how do the subsequent two proton-transfer processes proceed? Second, some key residues and the divalent cation have been proved to be crucial for the catalytic reaction of PC<sup>40–46</sup> and ODC,<sup>47</sup> but there is no detailed explanation about their roles. In addition, the energetics of the entire catalytic cycle is also not fully understood. It is known that a clear understanding of an enzymatic mechanism is helpful for regulating the enzyme's activity and for exploring the biocatalytic applications of enzymes and that some information cannot be acquired by experiments alone. Therefore, theoretical studies at the atomistic level are necessary. Yoshizawa et al. investigated the reaction mechanism of the BC domain by using the hybridized density functional theory method (B3LYP).<sup>48</sup> However, it is somewhat surprising that there is no theoretical study concerning the reaction mechanism of the CT domain.

Here, we employed the combined quantum-mechanics/molecular-mechanics (QM/MM) method to explore the catalytic mechanism of the CT domain of PC. In this methodology, the whole system is divided into a QM region that is treated quantum mechanically and a MM region that is described by a MM force field. The QM region involves the formation and cleavage of chemical bonds, whereas the MM region represents the surrounding environment. Thus, in the QM/MM method, not only can the chemical reaction occurring in the active site be described but also the effect of the environment can be considered.<sup>49–52</sup> Recently, the QM/MM method has become increasingly popular and was successfully applied in the field of extended systems, including enzymes.<sup>53–57</sup> Herein, the enzymatic reaction mechanism of the CT domain was systematically studied using the QM/MM method. The binding structure, reaction mechanism, detailed energetic profile of the overall reaction, and structures of all of the intermediates and transition states along the reaction pathways are presented.

## COMPUTATIONAL METHODS

**Models.** Because our present study aims to understand the catalytic mechanism of the PC CT domain, the calculations should begin with the enzyme–substrate complex. However, it is generally difficult to crystallize a structure of an enzyme–substrate complex by experimental methods under regular

conditions because the enzyme–substrate complex usually converts directly to the enzyme–product complex. Therefore, our initial computational model was constructed from a *S. aureus* CT domain that binds with PYR, Mn<sup>2+</sup>, and BTI (PDB code: 3BG5).<sup>39</sup> Although several crystal structures of the PC CT domain have been obtained, this is the only full-length one and is thought to be suitable for the mechanical study of the PC CT domain. In this crystal structure, only the active site of chain C of the CT domain is bound with the BTI tethered to chain D of the BCCP domain. Thus, these two domains are included in our model. The crystal structure and active site are shown in Figure 2. It should be noted that in this crystal

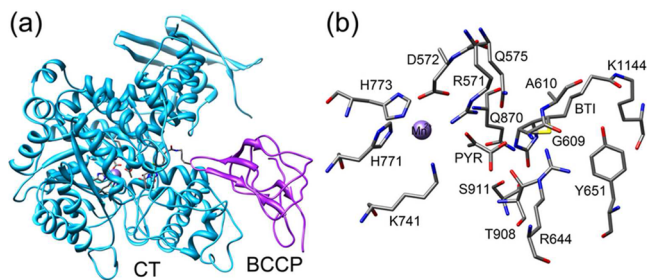


**Figure 2.** (a) Crystal structure of the CT domain of PC in complex with the BCCP domain (PDB code: 3BG5). (b) Active site pocket of the CT domain of PC.

structure the metal cation binding residue, K741, is not carbamylated (which is different from the equivalent lysine side chain in *R. etli* PC structures that is carbamylated<sup>45</sup>) in the human PC structure<sup>39</sup> and in the transcarboxylase structure.<sup>58</sup> Thus, the conclusions obtained in this article may be limited only to *S. aureus* PC and might not be universal for all PCs. However, these results may also provide some basic information for the catalytic mechanism of PCs from other species.

To recover the enzyme to its wild-type form, BTI was manually modified to CA-BTI. It has been known that in most vertebrate PCs the active site predominantly binds to Mn<sup>2+</sup>, whereas in that of yeast and bacteria PCs, Zn<sup>2+</sup> cation is the preferred metal cation.<sup>6,42,59</sup> Thus, the Zn<sup>2+</sup> cation, instead of the Mn<sup>2+</sup> cation, was used in our enzyme–substrate complex model. The protonation states of ionizable residues were determined according to the experimental conditions, and the pK<sub>a</sub> values were predicted by PROPKA 3.1 program.<sup>60</sup> Two Zn-coordinated histidine residues (H771 and H773) were determined to be their singly protonated states on  $\delta$  sites,

whereas Zn-coordinated residues K741 and D572 were set to their deprotonated states. Two other ionizable residues, R571 and R644, involved in the binding of PYR were modeled in their protonated states. The protonation states of all residues were checked carefully by the VMD program.<sup>61</sup> HBUILD in the CHARMM package was used to add hydrogen atoms of the residues.<sup>62</sup> Then, the obtained enzyme–substrate complex model was solvated into a water sphere with a 45 Å radius centered on the carboxyl carbon atom of CA-BTI to mimic the aqueous environment. The solvent was relaxed by a short MD simulation, and all of the other atoms were fixed. The final model thereby consists of 40 790 atoms after several Na<sup>+</sup> ions were randomly added to neutralize the system. To equilibrate the prepared system, a series of minimizations and a final 5 ns MD simulation were performed with stochastic boundary conditions<sup>63</sup> at 298 K and 1 atm. Such boundary conditions acts as a thermal bath to prevent the escape of water molecules from the dynamic region, preserving the properties of the system. The leapfrog integration scheme<sup>64</sup> was employed in all simulations with a time step of 1 fs. During the MD simulation, the system was divided into two regions: an outer buffer region (39 Å < r < 45 Å), where the atoms were treated by Langevin dynamics with friction and random force, and an inner reaction region (r < 39 Å), where the simulation was performed by Newton's equations of motion. The system can be kept at thermal equilibrium by using this hybrid method that couples the water molecules in the buffer region to a heat bath. The CHARMM22/CMAP all-atom force field<sup>65</sup> for the protein and the TIP3P model<sup>66</sup> for water molecules were employed. Because it is difficult to properly describe the zinc coordination shell by a MM force field,<sup>67–69</sup> the Zn<sup>2+</sup> cation was modeled with Stote's scheme,<sup>70</sup> and the Zn-coordinated residues were fixed to retain the zinc coordination structure during the MM minimizations and dynamics simulations.<sup>71</sup>

**QM/MM Calculations.** In the QM/MM calculations, the whole system was partitioned into two subsystems: QM and MM subsystems. As illustrated in Figure 3, the QM subsystem consists of those fragments that are potentially involved in the catalytic reaction, including residue T908; the side chains of R571, Q575, R644, T908, S911, K1144, and four Zn-coordinate residues (D572, H771, H773, and K741); CA-BTI; substrate PYR; and Zn<sup>2+</sup> cation. The QM region has a total of 133 atoms. In the description of the zinc coordination shell, the strategy utilized the Stuttgart ECP/basis set<sup>72</sup> (SDD) for the zinc atom and 6-31G(d) basis set for all other atoms, which has been previously tested and widely employed.<sup>71,73–75</sup> Because two proton-transfer processes are included in the catalytic reaction,

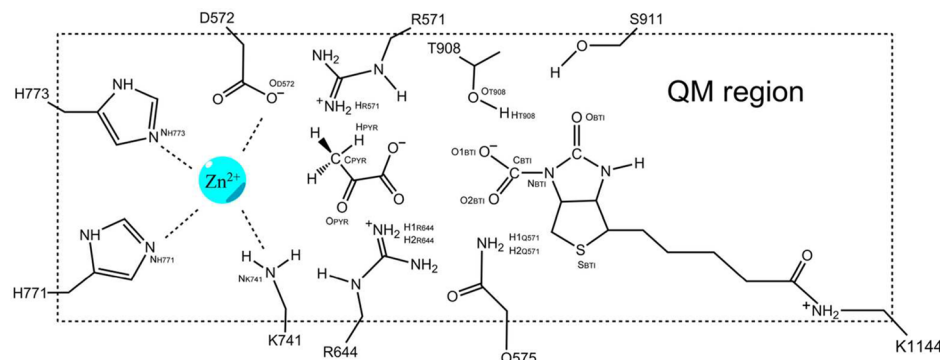


**Figure 3.** Selected quantum mechanics (QM) subsystem in the QM/MM calculations.

a higher level of B3LYP(SDD,6-31G(d,p)) was used in our calculations. All other residues and surrounding water molecules were set as the MM part and described by the CHARMM22 force field. The QM/MM boundaries were described by the link atom approach with a charge shift scheme.<sup>76,77</sup> The prepared QM/MM system was first minimized and then employed to map out the optimal energy paths with the reaction coordinate. The MM atoms within a distance of 16 Å from the substrate PYR were completely relaxed and fully optimized, whereas the remaining atoms were kept frozen. To avoid hyperpolarization of the QM wave function, the electronic embedding scheme was used to incorporate the MM point charges into the one-electron Hamiltonian of the QM calculation.<sup>78</sup> The QM/MM calculations were performed by the ChemShell package,<sup>79</sup> which incorporates the Turbomole module<sup>80</sup> and DL-POLY program<sup>81</sup> for the QM and MM regions, respectively. Geometry optimizations were implemented by the hybrid delocalized internal coordinates (HDLC) optimizer.<sup>82</sup> During the optimizations, the limited memory Broyden–Fletcher–Goldfarb–Shanno (L-BFGS) algorithm<sup>83,84</sup> was used to search for minima, and the partitioned rational function optimization (P-RFO) algorithm<sup>85</sup> was used for transition state search. The L-BFGS algorithm is a quasi-Newton method, and it approximates to the inverse Hessian matrix using a limited memory variation of the BFGS update. It is an excellent method for large-scale optimization and is well-suited for optimization problems with many variables. The P-RFO algorithm is Hessian eigenmode-following, and each found transition state is characterized by an unique negative eigenvalue.<sup>79</sup> There was no cutoff for the nonbonding MM and QM/MM interactions. Finally, high-level single-point electronic energy calculations were performed to obtain accurate energies at a larger basis set: B3LYP(SDD,6-31+ +G(d,p)) for the QM region and the CHARMM22/CMAP force field for the MM region. The frequency calculations were carried out at the level of B3LYP(SDD,6-31G(d,p)) for the QM region and CHARMM22/CMAP for the MM region using a two-point displacement method with analytical calculation of gradients.<sup>86</sup> During the frequency calculations, only the atoms of the QM region were included. However, the electronic polarization of the environment (MM region) is also considered, following the adiabatic approximation via complete self-consistent shell relaxation in the active MM region.<sup>86</sup> All reported energies are free energies from the large basis set with zero-point vibration energy corrections.

## ■ RESULTS AND DISCUSSION

**Structure of Enzyme–Substrate Complex.** Previous studies showed that the active sites of the PC and ODC CT domains are rearranged during substrate binding,<sup>42,47,87</sup> i.e., the active site adopts an open conformation in the absence of substrate and changes to a closed conformation upon PYR binding. The biotin binding pocket can be formed only after PYR binding.<sup>88,89</sup> In the present study, the initial model for the MD simulation was constructed on the basis of a structure in which the BTI of the BCCP domain is embedded into the CT domain, which is a catalytic state for PYR carboxylation. In this closed state, the binding site is relative stable and unlikely to undergo an obvious conformational change. This was also confirmed by our MD simulation. The root-mean-squared deviation (RMSD) of the protein during the MD simulation was derived and is shown in Figure S1. The dynamics trajectory

was stable after 2 ns, with a RMSD value of 2.1 Å, which reveals that the backbone of the protein changes only slightly.

It has been known that the initial structure can greatly influence the results of QM/MM calculations;<sup>90–92</sup> thus, its reasonable selection is a prerequisite for reliable results. A series of snapshots was taken as the QM/MM models from the MD simulation at intervals of 100 ps from 4 to 5 ns. These 11 models were first optimized by using the QM/MM method. As shown in the superposition of the optimized active sites (Figure S2), all of the changes of the protein residues are very small. From these geometries, a representative structure was chosen as the computational model for the following studies of reaction pathways, and the optimized solvated model and structure of the active site are shown in Figure 4. Compared with the crystal

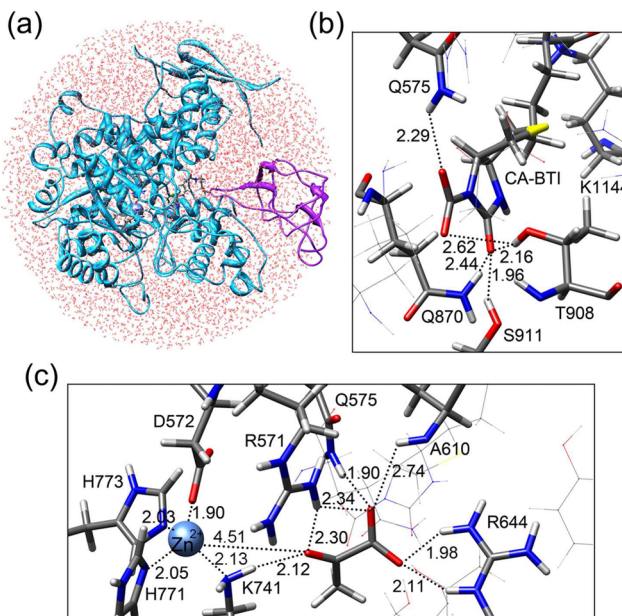


**Figure 4.** (a) QM/MM optimized solvated model. (b) Binding structure of BTI. (c) Binding structure of the  $Zn^{2+}$  cation and PYR. For clarity, only the residues that directly interact with BTI or  $Zn^{2+}$  and PYR are shown in stick models, whereas the other residues are shown in line models. The key distances are shown in angstroms.

structure, there are some slight deviations in the positions of the residues in the optimized structure. These differences are reasonable considering the fact that the crystal structure is the CT domain in complex with BTI rather than CA-BTI. During the QM/MM optimization, the  $Zn^{2+}$  cation is always coordinated with D572, K741, H771, and H773. In the optimized QM/MM model, the distances between the  $Zn^{2+}$  cation and the binding atoms of D572, K741, H771, and H773 are 1.90, 2.13, 2.05, and 2.03 Å, respectively, indicating a strong interaction of the  $Zn^{2+}$  cation with the coordinated residues, which is similar to that in the crystal structure. The carboxyl group of CA-BTI forms hydrogen bonds with the hydroxyl group of T908 and amino group of Q575, with lengths of 2.62 and 2.29 Å, respectively. Between the ureido group of CA-BTI and surrounding residues, three hydrogen bonds are formed. The lengths of these hydrogen bonds formed by the ureido oxygen atom with Q870, T908, and S911 are 2.44, 2.16, and 1.96 Å, respectively. These three residues may play important roles in stabilizing the negative charge of the ureido oxygen atom during the reaction.

It can be seen from Figure 4 that several residues are positioned in close proximity to substrate PYR. The glutamine/arginine pair (R571 and Q575) is conserved in all CT domain structures,<sup>28</sup> indicating their possible roles in stabilizing the substrate. Furthermore, mutagenesis experiments have provided some evidence about the roles of these residues. Mutating R644 in *S. aureus* PC<sup>43</sup> resulted in a complete loss of enzyme activity, and mutation of Zn-binding lysine in PC, TC, and ODC abolished or greatly reduced the activity of pyruvate carboxylation.<sup>35,41,45,47,58</sup> In our QM/MM optimized structure of the *S. aureus* PC CT domain, residue R571 forms hydrogen bonds with the carboxyl group and carbonyl group of PYR, with lengths of 2.34 and 2.30 Å, respectively, and residue Q575 interacts with the PYR carboxyl group by hydrogen bond, with a length of 1.90 Å. In addition, the Zn-binding residue K741 also forms a hydrogen bond with the PYR carbonyl group, with a bond length of 2.12 Å, and residue R644 forms a bidentate interaction with the PYR carboxyl group, with hydrogen bond lengths of 1.98 and 2.11 Å. Thus, a residue cluster consisting of R571, Q575, R644, and K741 contributes to the substrate binding in the *S. aureus* PC CT domain. In addition, in our optimized structure, there is a weak hydrogen bond between the carboxyl group of PYR and the main-chain amide of residue A610. These hydrogen bonds form a large hydrogen-bonding network in the active site.

**Binding Mode of Substrate with Metal Cation.** By comparing the optimized enzyme–substrate complex with the crystal structure, we found that the interaction mode of substrate PYR with the metal cation changes slightly. In the crystal structure from *S. aureus* (Figure 5a), the carbonyl

metal cation plays an insignificant role in polarizing PYR, and the resulting negative charge on the carbonyl oxygen in the following step will be stabilized by K741. In the previous experimental studies,<sup>94,95</sup> the interaction between PYR and metal cation in the PC–PYR complex has been investigated by using a series of experimental technologies, such as electron paramagnetic resonance and nuclear magnetic resonance. These results also indicated that this enzyme forms a second sphere enzyme–metal–ligand–substrate complex, in which a water molecule inserts between the metal cation and substrate. In our optimized structure (Figure 4), due to the absence of a water molecule, the K741 residue mediates the interaction between the metal cation and the substrate.

Whether the metal cation directly interacts with PYR depends on the individual enzyme from different species.<sup>39,45,58</sup>

Currently, the crystal structures of the PC CT domain and its homologous TC 5S subunit binding with the substrate PYR from four species have been solved, including *S. aureus* PC (PDB code: 3BG5),<sup>39</sup> human PC (PDB code: 3BG3),<sup>39</sup> *R. etli* PC (PDB code: 4JX5),<sup>45</sup> and *Propionibacterium shermanii* TC (PDB code: 1RQH).<sup>58</sup> The interaction modes of PYRs with the metal cations and their surrounding residues are shown in Figure 5. In human PC (Figure 5b), the O<sub>PYR</sub> is 3.87 and 3.68 Å from the metal cation and the nitrogen atom of carbamylated lysine, respectively, which is similar to that in the crystal structure of *S. aureus* PC (Figure 5a). In these two crystal structures, the coordination of metal cation with PYR is an inner sphere interaction. However, in the crystal structures from *R. etli* and *P. shermanii* (Figure 5c,d), PYRs were found to interact directly with the metal cation-binding water molecules (W), with distances of 2.69 and 2.85 Å, respectively, and the distances between the O<sub>PYR</sub> atoms and metal cation are 4.57 and 4.45 Å, respectively, which means that the coordination of the metal cation with PYR is a second sphere interaction. It is similar to our optimized structure in which PYR forms a hydrogen bond of 2.12 Å with the amino group of zinc-binding lysine instead of directly interacting with the Zn<sup>2+</sup> cation.

**Reaction Pathways.** In this article, three possible pathways were investigated. In the first pathway, the reaction starts from the deprotonation of PYR methyl, and the corresponding pathway is called the “deprotonation first mechanism”. Because no titratable residue is found nearby to abstract the hydrogen atom of PYR methyl, T908 is assumed to be deprotonated first by either the ureido group or the carboxyl group of CA-BTI, and it serves as the general base. The second pathway is called the “cage intermediate mechanism”, in which a cage intermediate is formed by the attack of sulfur on the ureido carbon atom. Schemes of these two pathways are shown in Figure S3. The last pathway is the “decarboxylation first mechanism”, which is the generally accepted mechanism, as shown in Figure 1. On the basis of the structure of the enzyme–substrate complex, the reaction pathways were systematically studied using QM/MM calculations. On the basis of our calculations, the deprotonation first mechanism and the cage intermediate mechanism have been ruled out, and the decarboxylation first mechanism is suggested to be the most possible pathway.

In the deprotonation first mechanism, the sole residue responsible for the deprotonation of PYR methyl is T908. Therefore, T908 should be first deprotonated by either the ureido group or the carboxyl group of CA-BTI. These two proton transfers may occur in a concerted or stepwise manner. Thus, starting from the initial optimized structure, we scanned

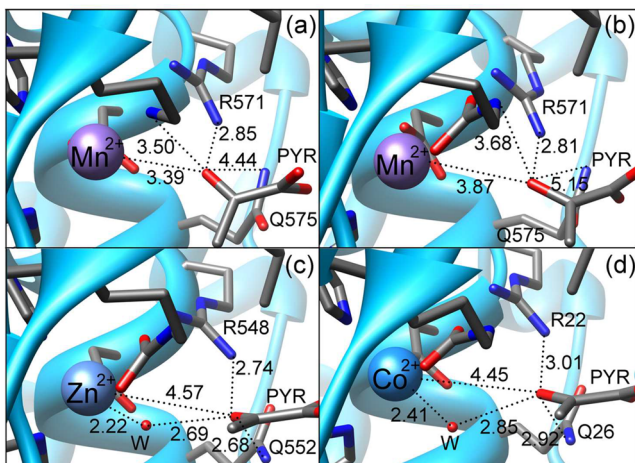


**Figure 5.** Interaction modes between PYR, metal cation, and some surrounding residues from four species: (a) *S. aureus* (PDB code: 3BG5), (b) human (PDB code: 3BG3), (c) *Rhizobium etli* (PDB code: 4JX5), and (d) *Propionibacterium shermanii* (PDB code: 1RQH). The key distances are given in angstroms.

oxygen atom of PYR (O<sub>PYR</sub>) interacts weakly with the Mn<sup>2+</sup> metal cation, with a distance of 3.39 Å. However, in our optimized enzyme–substrate complex, the distance between O<sub>PYR</sub> and the Zn<sup>2+</sup> cation increases to 4.51 Å, and a hydrogen bond is formed between PYR and K741, with a length of 2.12 Å. This change may be caused by the flexibility of zinc coordination.<sup>75,93</sup> Our optimized structure suggests that the coordination of the metal cation with PYR is a second sphere rather than an inner sphere interaction, indicating that the

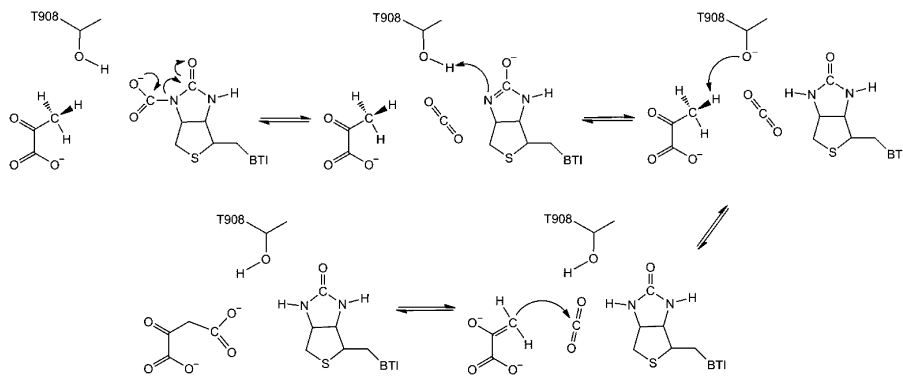


**Figure 6.** Proposed catalytic mechanism of the CT domain of PC based on our calculations.

two reaction coordinates defined as  $\text{RC}=\text{r}(\text{O}_{\text{BTI}}-\text{H}_{\text{T908}})$  and  $\text{RC}=\text{r}(\text{O1}_{\text{BTI}}-\text{H}_{\text{T908}})$  for the deprotonation of T908 in the stepwise mechanism and two reaction coordinates defined as  $\text{RC}=\text{r}(\text{C}_{\text{PYR}}-\text{H}_{\text{PYR}})-\text{r}(\text{H}_{\text{T908}}-\text{O}_{\text{BTI}})$  and  $\text{RC}=\text{r}(\text{C}_{\text{PYR}}-\text{H}_{\text{PYR}})-\text{r}(\text{H}_{\text{T908}}-\text{O1}_{\text{BTI}})$  for the concerted mechanism. For the cage intermediate mechanism, we scanned the reaction coordinate defined as  $\text{RC}=\text{r}(\text{C}_{\text{BTI}}-\text{S}_{\text{BTI}})$ . In these two pathways, along the reaction coordinates the calculated energies were continuously increased, and no saddle points were found (as shown in Figure S4–S8). In the decarboxylation first mechanism, we found that the two proton-transfer processes (from T908 to enol-BTI and from PYR to T908) proceed in a stepwise manner. Thus, the entire reaction contains four elementary steps, as shown in Figure 6. To clearly elucidate the catalytic cycle, the reaction is described as three parts: (1) the decarboxylation of CA-BTI, (2) the proton-transfer processes, and (3) the carboxylation of enol-PYR. They will each be discussed in turn in the following sections. The optimized structures and key parameters of the reactant (R), transition states (TS1–TS4), intermediates (IM1–IM3), and product (P) are shown in Figure 7. For the sake of clarity, CA-BTI, PYR, and T908 are given in ball and stick models in the figure. The atomic coordinates of the QM region of all optimized structures are given in the Supporting Information.

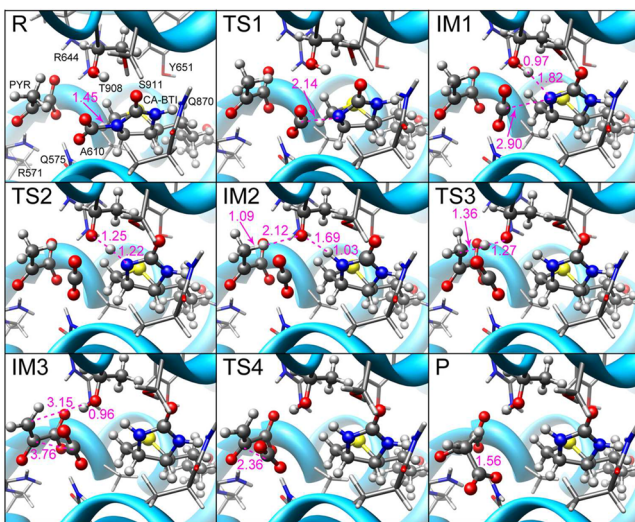


**Figure 7.** Optimized geometries for various species. For clarity, CA-BTI, PYR, and T908 are shown in ball and stick models. The key bond distances are given in angstroms.

**Decarboxylation of CA-BTI.** As proposed previously, the decarboxylation of CA-BTI in the CT domain occurs prior to the proton transfer,<sup>29–31,40–42</sup> and an enol-BTI intermediate is formed first. As shown in Figure 7, from reactant R to transition state TS1, the  $\text{C}_{\text{BTI}}-\text{N}_{\text{BTI}}$  bond is gradually weakened, with the bond length changing from 1.45 to 2.14 Å. Downhill from TS1 to IM1, this bond length further increases to 2.90 Å, which means that the  $\text{C}_{\text{BTI}}-\text{N}_{\text{BTI}}$  bond has been completely cleaved and the anionic enol-BTI intermediate has been formed. Previous experimental studies suggested that the decarboxylation of CA-BTI is at least partially rate limiting.<sup>37,96</sup> In our calculations, this step is calculated to be rate-limiting, with the highest free energy barrier of 21.7 kcal/mol (Figure 8), which

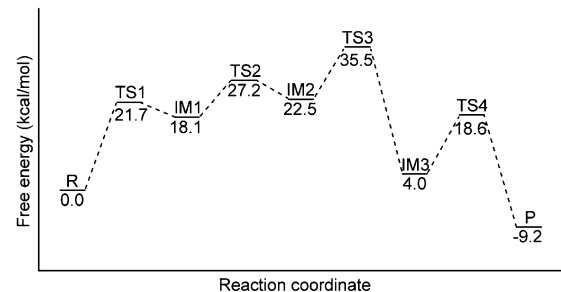


**Figure 8.** Free energy profiles of the CT domain of the PC catalytic reaction.

agrees well with the experimental suggestion. The calculated free energy changes ( $\Delta G$ ), enthalpies and enthalpy changes ( $H$ ,  $\Delta H$ ), and entropies ( $S$ ) are given in Table S1. In this elementary step, the contribution of the entropic effect to the free energy barrier is negligible. However, in intermediate IM1,  $\Delta G$  is 1.6 kcal/mol lower than that of  $\Delta H$ , indicating that the entropic effect has a minor influence on  $\Delta G$  of the species where  $\text{CO}_2$  is present. Overall, the contributions of the entropic effect to the free energy changes are very small, as can be seen in the following elementary steps.

In addition, the enol-BTI intermediate is 18.1 kcal/mol higher than R in energy, indicating that this intermediate is a highly reactive species. The formation of the enol-BTI intermediate is mainly due to the hydrogen bonds between the ureido oxygen atom,  $\text{O}_{\text{BTI}}$ , and surrounding residues. In the enzyme–substrate complex, residues Q870 and S911 form hydrogen bonds with CA-BTI, with bond lengths of 2.44 and 1.96 Å, respectively. Both of these hydrogen bonds are strengthened in the enol-BTI intermediate, with their bond lengths decreasing to 1.91 and 1.83 Å, respectively. Thus,

residues Q870 and S911 contribute significantly to the stabilization of anionic enol-BTI, which is in accordance with the experimental suggestions.<sup>39,41</sup>

Because this decarboxylation process corresponds to a high energy barrier and generates a highly reactive intermediate, IM1, we further investigated a concerted mechanism in which the decarboxylation of CA-BTI occurs in concert with the proton transfer from T908 to CA-BTI. The concerted reaction was scanned with the reaction coordinate as a combination of two bond lengths:  $RC=r(C_{BTI}-N_{BTI})-r(N_{BTI}-H_{T908})$ . Interestingly, during the scanning of  $r(C_{BTI}-N_{BTI})$  from 1.45 to 3.50 Å, only the  $C_{BTI}-N_{BTI}$  bond changed along the reaction coordinate, whereas the hydrogen atom of T908 was always attached steadily, indicating that these two processes take place step by step and that the decarboxylation takes place prior to the proton transfer. Furthermore, to deeply understand this stepwise mechanism, the potential energy surface (PES) as a function of distances  $r_1 (C_{BTI}-N_{BTI})$  and  $r_2 (H_{T908}-N_{BTI})$  was also mapped out using the adiabatic mapping approach at the level of B3LYP(SDD,6-31G(d,p)) for the QM region and using the CHARMM22/CMAP force field for the MM region, as shown in Figure 9. To save computational resources, residues

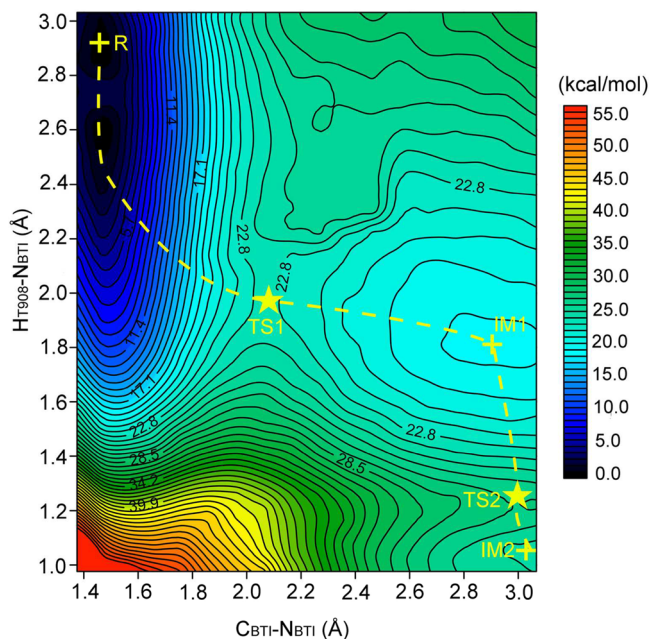


**Figure 9.** PES calculated at the level of B3LYP(SDD,6-31G(d,p)) for the QM region and using the CHARMM22/CMAP force field for the MM region, using distances  $r_1 (C_{BTI}-N_{BTI})$  and  $r_2 (H_{T908}-N_{BTI})$  as reaction coordinates.

R571 and Q575, which do not directly participate in the reaction but only form hydrogen bonds with the substrate, were not included in the QM region. The PES characterizes the cleavage of the  $C_{BTI}-N_{BTI}$  bond and the proton transfer from residue T908 to the  $N_{BTI}$  atom of CA-BTI. The vertical and horizontal axes describe the cleavage of the  $C_{BTI}-N_{BTI}$  bond and the proton transfer from T908 to CA-BTI, respectively. The reaction coordinates are changed by a decrement of 0.05 Å for  $r_1 (C_{BTI}-N_{BTI})$  and increment of 0.08 Å for  $r_2 (H_{T908}-N_{BTI})$ . From Figure 9, three energy minima can be recognized on the entire PES. A careful examination of the geometrical parameters reveals that the minima in the upper-left and lower-right corners correspond to the reactant R and intermediate IM2,

respectively, and that the other minimum corresponds to the intermediate IM1. Thus, from R to IM2, the reaction should undergo two transition states, i.e., the cleavage of the  $C_{BTI}-N_{BTI}$  bond and the proton transfer, which proceed in a stepwise manner.

**Proton-Transfer Processes.** After the formation of enol-BTI intermediate, the reaction undergoes two proton-transfer processes (from T908 to enol-BTI and from PYR to T908). From the optimized structure of IM1 in Figure 7, one can see that  $H_{T908}$  is 1.82 Å away from the  $N_{BTI}$  atom of enol-BTI, which changes to 1.22 Å in TS2. In IM2, this distance further shortens to 1.03 Å, indicating the complete formation of the  $N_{BTI}-H_{T908}$  bond. In this intermediate, the proton of T908 has transferred to the  $N_{BTI}$  atom of BTI, whereas the hydrogen atom of the PYR methyl group is still attached. Subsequently, from IM2 to IM3 via TS3, the distance between  $H_{PYR}$  and  $O_{T908}$  decreases from 2.12 to 0.96 Å via 1.27 Å, indicating the completion of two proton-transfer processes to form an enol-PYR intermediate characterized by  $sp^2$ -hybridized carbon atoms. Our calculation results indicate that the two proton-transfer processes follow a stepwise mechanism. Zeczycki et al. once suggested that an unstable threonine alkoxide intermediate can be avoided if the two proton-shift processes occur concertedly.<sup>41</sup> However, from the optimized structure of the threonine alkoxide intermediate (IM2) in Figure 7, one can see that residue T908 forms two hydrogen bonds with the methyl groups of PYR and BTI, with bond lengths of 2.12 and 1.69 Å, respectively. These hydrogen bonds stabilize the highly reactive T908-alkoxide intermediate, thereby leading to the formation of IM2.

As shown in Figure 8, the first proton-transfer process is calculated to occur easily, with an energy barrier of 9.1 kcal/mol. The formed T908-alkoxide intermediate is 22.5 kcal/mol higher than R in energy, and the following proton-transfer process corresponds to a low energy barrier of 13.0 kcal/mol, indicating that this intermediate is a stable but highly reactive species. Thus, it is possible to experimentally observe a concerted, but highly asynchronous, two proton-transfer process. In addition, the energy of IM3 is 18.5 kcal/mol lower than that of IM2 and 14.1 kcal/mol lower than that of IM1. Thus, IM3 is a stable intermediate in the course of the reaction. From Table 1, it can be seen that in intermediate IM3 all hydrogen bond lengths formed by PYR and residues K741, R571, and Q575 are shortened, whereas those formed by PYR and R644 are nearly constant, indicating that residues K741, R571, and Q575, rather than R644, play important roles in stabilizing the enol-PYR intermediate. Therefore, we conjecture that mutating the glutamine/arginine pair (R571 and Q575) may not influence the substrate binding but will significantly affect the stability of the enol-PYR intermediate, which agrees with the experimental studies on *R. etli* PC.<sup>44</sup> In addition, the relative energy of TS3 is 35.5 kcal/mol higher than that of R, which is the highest point in the energy profile, indicating that the calculated energy barrier of the entire reaction is 35.5 kcal/mol. This value is much larger than that estimated from the experimental data ( $k_{cat} = 6.5 \text{ s}^{-1}$ ), 16.3 kcal/mol,<sup>43</sup> which may be caused by the limitations of the computational methods used here. First, only one configuration of the reactant was used to map out the reaction pathway. Second, the obtained energy of each species is based on a single structure without including conformational sampling. In addition, the functional that was used may also influence the energetics of the reaction. Thus, the predicted energetics may not provide a direct comparison

**Table 1.** Key Distances<sup>a</sup> in the Optimized Structures of All Species Involved in the Reaction

	R	TS1	IM1	TS2	IM2	TS3	IM3	TS4	P
d(H <sub>K741</sub> –O <sub>PYR</sub> )	2.12	2.07	2.20	2.23	2.26	2.36	1.91	2.02	2.07
d(H <sub>R571</sub> –O <sub>PYR</sub> )	2.30	2.41	2.21	2.19	2.16	2.08	1.86	1.95	2.42
d(H <sub>R571</sub> –O <sub>1_PYR</sub> )	2.34	2.26	2.47	2.49	2.55	2.62	2.41	2.38	2.17
d(H <sub>Q575</sub> –O <sub>1_PYR</sub> )	1.89	1.89	1.90	1.88	1.87	1.85	1.82	1.85	1.95
d(H <sub>1_R644</sub> –O <sub>2_PYR</sub> )	2.11	2.12	2.11	2.12	2.11	2.02	2.26	2.27	2.37
d(H <sub>2_R644</sub> –O <sub>2_PYR</sub> )	1.98	2.00	2.01	1.97	1.97	1.90	1.94	1.98	2.14
d(H <sub>Q870</sub> –O <sub>BTI</sub> )	2.44	2.09	1.91	2.04	2.03	2.33	2.53	2.43	2.43
d(H <sub>S911</sub> –O <sub>BTI</sub> )	1.96	1.89	1.83	1.94	2.01	2.02	2.03	2.01	2.00
d(H <sub>K912</sub> –O <sub>BTI</sub> )	4.65	4.51	3.73	3.67	3.65	3.66	3.70	3.70	3.72
d(HN <sub>Q870</sub> –O <sub>1_BTI</sub> )	3.36	3.62	4.59	4.67	4.78	4.97	5.07	4.70	3.45
d(HN <sub>Q870</sub> –O <sub>2_BTI</sub> )	3.64	3.72	3.44	3.59	3.67	3.42	3.64	3.97	3.84
d(H <sub>2_Q575</sub> –O <sub>2_BTI</sub> )	2.29	2.55	3.66	3.69	3.68	3.95	3.76	3.26	2.24
d(HN <sub>T908</sub> –O <sub>1_BTI</sub> )	3.53	3.42	2.54	2.45	2.42	2.53	2.69	3.42	5.37
d(Zn–O <sub>D572</sub> )	1.90	1.90	1.89	1.90	1.89	1.90	1.90	1.90	1.92
d(Zn–N <sub>K741</sub> )	2.13	2.13	2.15	2.15	2.15	2.16	2.10	2.11	2.10
d(Zn–N <sub>H771</sub> )	2.05	2.05	2.04	2.04	2.04	2.04	2.06	2.05	2.07
d(Zn–N <sub>H773</sub> )	2.03	2.03	2.03	2.04	2.04	2.05	2.06	2.04	2.02

<sup>a</sup>Distances are given in angstroms.

with the experimental value. However, as referenced in some literature,<sup>97–100</sup> these limitations can not change the reaction pathways, implying that these calculated results are still meaningful for us to understand the catalytic mechanism.

To further understand proton-transfer processes, PES as a function of the distances of r3 (H<sub>T908</sub>–N<sub>BTI</sub>) and r4 (C<sub>PYR</sub>–H<sub>PYR</sub>) was also mapped out, which is shown in Figure 10. During the scanning, residues R571 and Q575 were also not

included in the QM region. The vertical axis describes the proton transfer from PYR to T908, and the horizontal axis designates the proton transfer from T908 to enol-BTI. The reaction coordinates were changed by a decrement of 0.05 Å for r3 (H<sub>T908</sub>–N<sub>BTI</sub>) and an increment of 0.05 Å for r4 (C<sub>PYR</sub>–H<sub>PYR</sub>). In Figure 10, the lower-right corner represents intermediate IM1, whereas the lower-left and upper-left corners correspond to intermediates IM2 and IM3, respectively. From Figure 10, a stepwise mechanism for the two proton-transfer processes can be easily concluded.

**Carboxylation of PYR.** The last step of the overall reaction is the nucleophilic attack of enol-PYR on the carbon atom of CO<sub>2</sub>. In IM3, the carbon atom of CO<sub>2</sub> is located at 3.76 Å from the C<sub>PYR</sub> atom of PYR. The last transition state (TS4) was characterized by a C<sub>BTI</sub>–C<sub>PYR</sub> distance of 2.36 Å, as shown in Figure 7. Beyond transition state TS4, the product is generated with a single C<sub>BTI</sub>–C<sub>PYR</sub> bond of 1.56 Å. This nucleophilic attack corresponds to an energy barrier of 14.6 kcal/mol. The product P is 9.2 kcal/mol lower than the reactant R in energy, indicating that the overall reaction is exothermic.

**Role of Key Residues and Zn-Binding Site.** Previous experimental studies suggested that the side-chain hydroxyl of S911 and the main-chain amide of K912 form hydrogen bonds with the carbonyl oxygen of BTI (O<sub>BTI</sub>).<sup>39</sup> In the crystal structure (PDB code: 3BG5), O<sub>BTI</sub> is 2.54 and 3.10 Å from the oxygen atom of the side-chain hydroxyl group of S911 and the nitrogen atom of the main-chain amide group of K912, respectively. In addition, the nitrogen atom N<sub>e</sub> of Q870 is in close proximity to the O<sub>BTI</sub> atom, with a distance of 3.96 Å. In our optimized enzyme–substrate complex, the hydrogen atom (H<sub>K912</sub>) attached to the N atom of the main-chain amide of K912 is located in an unfavorable orientation for forming a hydrogen bond with BTI. As shown in Figure 11, the distance (d<sub>3</sub>) between O<sub>BTI</sub> of BTI and H<sub>K912</sub> of K912 is 4.65 Å. However, the other two residues, Q870 and S911, interact with O<sub>BTI</sub> of BTI by hydrogen bonds, with lengths (d<sub>1</sub> and d<sub>2</sub>) of 2.44 and 1.96 Å, respectively. For comparison, the values of d<sub>1</sub>–d<sub>3</sub> in the optimized structures of all species are listed in Table 1. During the reaction course, the hydrogen bonds formed by S911 and Q870 with BTI remain stable, but K912 always weakly interacts with BTI. Nevertheless, d<sub>1</sub> and d<sub>2</sub> are

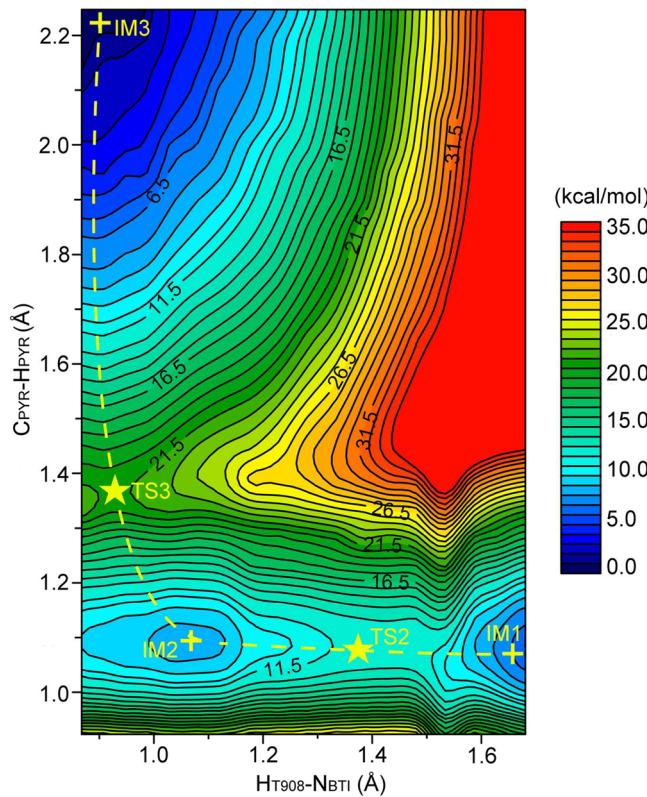


**Figure 10.** PES calculated at the level of B3LYP(SDD,6-31G(d,p)) for the QM region and using the CHARMM22/CMAP force field for the MM region, using distances r3 (H<sub>T908</sub>–N<sub>BTI</sub>) and r4 (C<sub>PYR</sub>–H<sub>PYR</sub>) as reaction coordinates.

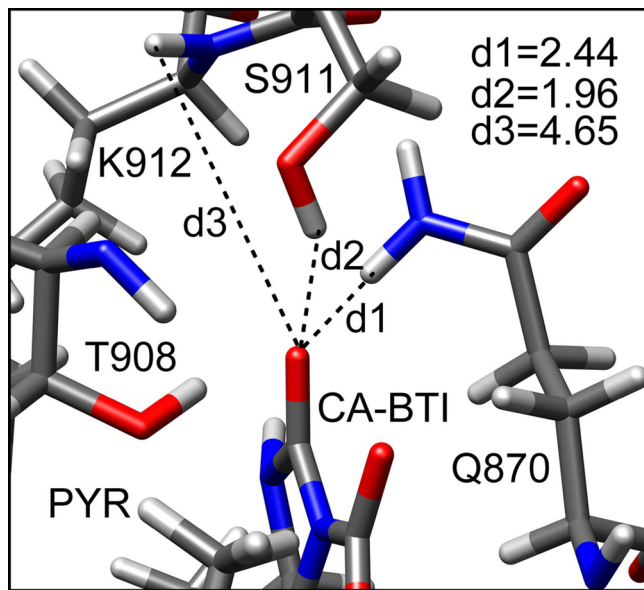


**Figure 11.** Interactions of the ureido oxygen atom with the side-chain hydroxyl of S911 and Q870 and the main-chain amide of K912 in the optimized enzyme–substrate complex. The key distances are given in angstroms.

clearly shortened in the structures of intermediates and transition states where BTI is in its hydroxyl anion form. Thus, we can conclude that the oxyanion hole, consisting of the side-chain hydroxyl of S911 and the side-chain amino of Q870, plays an important role in stabilizing the hydroxyl anion of BTI in the reaction, which can facilitate proton transfer from T908 to the  $\text{N}_{\text{BTI}}$  atom of BTI. This agrees well with the suggestion based on the experimental data.<sup>39,41</sup>

The  $\text{CO}_2$  formed in the first step should be trapped to prevent its escape from the active site. In the optimized enzyme–substrate complex, several residues may play this role, including Q575, Q870, and T908. The distances between the hydrogen atom ( $\text{H}_{\text{N}_{\text{Q870}}}$ ) of the main-chain amide of Q870 and two carboxyl oxygen atoms ( $\text{O}_{1\text{-BTI}}$  and  $\text{O}_{2\text{-BTI}}$ ) of CA-BTI are 3.36 and 3.64 Å, respectively. The hydrogen atom ( $\text{H}_{\text{Q575}}$ ) of the side-chain amide of Q575 is located 2.29 Å from the oxygen atom ( $\text{O}_{2\text{-BTI}}$ ) of CA-BTI, and the hydrogen atom ( $\text{H}_{\text{T908}}$ ) of the main-chain amide of T908 is 3.53 Å from the oxygen atom ( $\text{O}_{1\text{-BTI}}$ ) of CA-BTI. These distances in the species of the reaction pathway are given in Table 1. One can see that in the species with the presence of  $\text{CO}_2$  the distance  $d(\text{H}_{\text{N}_{\text{T908}}}-\text{O}_{1\text{-BTI}})$  is obviously shortened, the distances of  $d(\text{H}_{\text{N}_{\text{Q870}}}-\text{O}_{1\text{-BTI}})$  and  $d(\text{H}_{\text{Q575}}-\text{O}_{2\text{-BTI}})$  are nearly constant, and the distance  $d(\text{H}_{\text{Q575}}-\text{O}_{2\text{-BTI}})$  is lengthened, which means that the main-chain amide of T908 plays a key role in stabilizing  $\text{CO}_2$ .

The metal cation-binding site in the CT domain has been proved to be critical in PC, ODC, and TC. For these three

enzymes, mutation of coordinated residues can greatly reduce or completely eliminate their activity,<sup>35,41,45,47,94,95</sup> and removal of the metal cation can lead to the dissociation of the enzyme.<sup>101–103</sup> Thus, the whole metal cation-binding site may play an important role in stabilizing the structure of the enzyme. In this article, the role of the Zn-binding site in the PC CT domain was further explored. The ESP charges of the zinc cation and its ligands are given in Table 2. During the entire reaction process, these charges remain unchanged, indicating that the zinc cation does not function as a Lewis acid to influence the reaction. In the previous studies of the *P. shermanii* TC SS<sup>58</sup> and *R. etli* PC CT domains,<sup>46</sup> the consistent conclusion that the metal cation does not act as a Lewis acid was also obtained. In addition, the distances between the  $\text{Zn}^{2+}$  cation and its coordinated atoms are listed in Table 1. It can be seen that the coordination bonds between the zinc cation and its ligands are unperturbed during the reaction but that the length of hydrogen bond formed by PYR and K741 changes along the reaction coordinate and has a minimum in enol-PYR intermediate IM3. Thus, we can conclude that the metal cation may play a role in stabilizing the reaction species through mediator residue K741 in the *S. aureus* PC CT domain.

## CONCLUSIONS

In this article, the catalytic mechanism of the CT domain of PC from *S. aureus* was investigated using a combined QM/MM approach. The calculation results indicate that the entire catalytic cycle contains four elementary steps. The reaction starts from the decarboxylation of CA-BTI to generate an enol-BTI intermediate, which is followed by two stepwise proton-transfer processes (from T908 to enol-BTI and from PYR to T908). Then, the product, oxaloacetate, is formed by the nucleophilic attack of enol-PYR on the previously generated  $\text{CO}_2$ . Residue T908 acts as the general acid/base to protonate enol-BTI and to abstract the hydrogen atom of the PYR methyl group. In addition, the main-chain amide of T908 plays a key role in catching  $\text{CO}_2$  and preventing its diffusion from the active center. A triad of R571, Q575, and K741 contributes both to substrate binding and enol-pyruvate stabilization, and residue R644 contributes only to substrate binding. The oxyanion hole, consisting of the side-chain hydroxyl of S911 and the side-chain amino of Q870, plays important role in stabilizing the hydroxyl anion of BTI, which facilitates the proton transfer from T908 to enol-BTI. The coordination of the metal cation by PYR is a second sphere, rather than an inner sphere, interaction, and the metal cation plays a stabilizing function by a mediator residue, K741. At the level of B3LYP(SDD,6-31++G(d,p))/B3LYP(SDD,6-31G(d,p)) for the QM region and using the CHARMM22/CMAP force field for the MM region, the decarboxylation of carboxybiotin corresponds to the highest energy barrier of 21.7 kcal/mol, which agrees with the experimental suggestion. Our results may

**Table 2. ESP Charges of the  $\text{Zn}^{2+}$  Cation and Zn-Coordinated Residues in the Optimized Structures of All Species Involved in the Reaction**

	R	TS1	IM1	TS2	IM2	TS3	IM3	TS4	P
$\text{Zn}^{2+}$	0.98	0.98	0.97	0.97	0.97	0.96	0.96	0.97	0.98
D572	-0.92	-0.91	-0.91	-0.91	-0.92	-0.92	-0.91	-0.92	-0.91
K741	0.09	0.08	0.08	0.09	0.09	0.11	0.10	0.17	0.11
H771	0.05	0.06	0.05	0.07	0.05	0.06	0.06	0.04	0.02
H774	0.09	0.08	0.08	0.09	0.08	0.08	0.07	0.08	0.10

provide useful information for the regulation of enzyme activity and for the enzymatic redesign of biocatalytic applications.

## ASSOCIATED CONTENT

### Supporting Information

Summary of the calculated free energy changes ( $\Delta G$ ), enthalpies and enthalpy changes ( $H$ ,  $\Delta H$ ), and entropies ( $S$ ) of structures of all species involved in the reaction; time dependence of RMSD from 5 ns MD simulations; superposition of the active sites of initial optimized geometries; schematic illustrations of the deprotonation first mechanism and cage intermediate mechanism of the PC CT domain catalytic reaction; calculated energy profiles along the reaction coordinates of  $RC=r(O_{BTI}-H_{T908})$ ,  $RC=r(O1_{BTI}-H_{T908})$ ,  $RC=r(C_{PYR}-H_{PYR})-r(H_{T908}-O_{BTI})$ ,  $RC=r(C_{PYR}-H_{PYR})-r(H_{T908}-O1_{BTI})$ , and  $RC=r(C_{BTI}-S_{BTI})$ ; atomic coordinates of QM region of all optimized structures. This material is available free of charge via the Internet at <http://pubs.acs.org>.

## AUTHOR INFORMATION

### Corresponding Author

\*Tel.: +86 531 883 655 76. Fax: +86 531 885 644 64. E-mail: [yongjunliu\\_1@sdu.edu.cn](mailto:yongjunliu_1@sdu.edu.cn).

### Funding

This work was supported by the National Natural Science Foundation of China (21173129 and 21373125).

### Notes

The authors declare no competing financial interest.

## ABBREVIATIONS USED

PC, pyruvate carboxylase; BTI, biotin; PYR, pyruvate; BC, biotin carboxylase; CT, carboxyl transferase; BCCP, biotin carboxyl carrier protein; CA-BTI, carboxybiotin; ODC, oxaloacetate decarboxylase; TC, transcarboxylase; PT, PC tetramerization

## REFERENCES

- (1) Jitrapakdee, S., Vidal-Puig, A., and Wallace, J. C. (2006) Anaplerotic roles of pyruvate carboxylase in mammalian tissues. *Cell. Mol. Life Sci.* 63, 843–854.
- (2) Wallace, J. C. (2010) My favorite carboxylase. *IUBMB Life* 62, 535–538.
- (3) Waldrop, G. L., Holden, H. M., and St. Maurice, M. (2012) The enzymes of biotin dependent  $CO_2$  metabolism: what structures reveal about their reaction mechanisms. *Protein Sci.* 21, 1597–1619.
- (4) Adina-Zada, A., Zeczycki, T. N., St. Maurice, M., Jitrapakdee, S., Cleland, W. W., and Attwood, P. V. (2012) Allosteric regulation of the biotin-dependent enzyme pyruvate carboxylase by acetyl-CoA. *Biochem. Soc. Trans.* 40, 567–572.
- (5) Tong, L. (2013) Structure and function of biotin-dependent carboxylases. *Cell. Mol. Life Sci.* 70, 863–891.
- (6) Wallace, J. C., and Easterbrook-Smith, S. B. (1985) *Pyruvate Carboxylase* (Keech, D. B., and Wallace, J. C., Eds.) pp 65–107, CRC Press, Boca Raton, FL.
- (7) Wurtele, E. S., and Nikolau, B. J. (1990) Plants contain multiple biotin enzymes: discovery of 3-methylcrotonyl-CoA carboxylase, propionyl-CoA carboxylase and pyruvate carboxylase in the plant kingdom. *Arch. Biochem. Biophys.* 278, 179–186.
- (8) Freytag, S. O., and Utter, M. F. (1980) Induction of pyruvate carboxylase apoenzyme and holoenzyme in 3T3-L1 cells during differentiation. *Proc. Natl. Acad. Sci. U.S.A.* 77, 1321–1325.
- (9) Gamberino, W. C., Berkich, D. A., Lynch, C. J., Xu, B., and LaNoue, K. F. (1997) Role of pyruvate carboxylase in facilitation of synthesis of glutamate and glutamine in cultured astrocytes. *J. Neurochem.* 69, 2312–2325.
- (10) Large, V., and Beylot, M. (1999) Modifications of citric acid cycle activity and gluconeogenesis in streptozotocin-induced diabetes and effects of metformin. *Diabetes* 48, 1251–1257.
- (11) Lu, D., Mulder, H., Zhao, P., Burgess, S. C., Jensen, M. V., Kamzolova, S., Newgard, C. B., and Sherry, A. D. (2002)  $^{13}C$  NMR isotopomer analysis reveals a connection between pyruvate cycling and glucose-stimulated insulin secretion (GSIS). *Proc. Natl. Acad. Sci. U.S.A.* 99, 2708–2713.
- (12) Reshef, L., Olswang, Y., Cassuto, H., Blum, B., Croniger, C. M., Kalhan, S. C., Tilghman, S. M., and Hanson, R. W. (2003) Glyceroneogenesis and the triglyceride/fatty acid cycle. *J. Biol. Chem.* 278, 30413–30416.
- (13) Fan, T. W., Lane, A. N., Higashi, R. M., Farag, M. A., Gao, H., Bousamra, M., and Miller, D. M. (2009) Altered regulation of metabolic pathways in human lung cancer discerned by  $(13)C$  stable isotope-resolved metabolomics (SIRM). *Mol. Cancer* 8, 41.
- (14) Cheng, T., Sudderth, J., Yang, C., Mullen, A. R., Jin, E. S., Matés, J. M., and DeBerardinis, R. J. (2011) Pyruvate carboxylase is required for glutamine-independent growth of tumor cells. *Proc. Natl. Acad. Sci. U.S.A.* 108, 8674–8679.
- (15) MacDonald, M. J., Longacre, M. J., Langberg, E. C., Tibell, A., Kendrick, M. A., Fukao, T., and Ostenson, C. G. (2009) Decreased levels of metabolic enzymes in pancreatic islets of patients with type 2 diabetes. *Diabetologia* 52, 1087–1091.
- (16) Han, J., and Liu, Y. Q. (2010) Reduction of islet pyruvate carboxylase activity might be related to the development of type 2 diabetes mellitus in Agouti-K mice. *J. Endocrinol.* 204, 143–152.
- (17) Jitrapakdee, S., Wutthisathapornchai, A., Wallace, J. C., and MacDonald, M. J. (2010) Regulation of insulin secretion: role of mitochondrial signaling. *Diabetologia* 53, 1019–1032.
- (18) Lee, P., Leong, W., Tan, T., Lim, M., Han, W., and Radda, G. K. (2013) *In vivo* hyperpolarized carbon-13 magnetic resonance spectroscopy reveals increased pyruvate carboxylase flux in an insulin-resistant mouse model. *Hepatology* 57, 515–524.
- (19) Kumashiro, N., Beddow, S. A., Vatner, D. F., Majumdar, S. K., Cantley, J. L., Guebre-Egziabher, F., Fat, I., Guigni, B., Jurczak, M. J., Birkenfeld, A. L., Kahn, M., Perler, B. K., Puchowicz, M. A., Manchem, V. P., Bhanot, S., Still, C. D., Gerhard, G. S., Petersen, K. F., Cline, G. W., Shulman, G. I., and Samuel, V. T. (2013) Targeting pyruvate carboxylase reduces gluconeogenesis and adiposity and improves insulin resistance. *Diabetes* 62, 2183–2194.
- (20) Jeoung, N. H., Harris, C. R., and Harris, R. A. (2014) Regulation of pyruvate metabolism in metabolic-related diseases. *Rev. Endocr. Metab. Disord.* 15, 99–110.
- (21) Mochel, F., DeLonlay, P., Touati, G., Brunengraber, H., Kinman, R. P., Rabier, D., Roe, C. R., and Saudubray, J. M. (2005) Pyruvate carboxylase deficiency: clinical and biochemical response to anaplerotic diet therapy. *Mol. Genet. Metab.* 84, 305–312.
- (22) Monnot, S., Serre, V., Chadefaux-Vekemans, B., Aupetit, J., Romano, S., De Lonlay, P., Rival, J. M., Munnich, A., Steffann, J., and Bonnefont, J. P. (2009) Structural insights on pathogenic effects of novel mutations causing pyruvate carboxylase deficiency. *Hum. Mutat.* 30, 734–740.
- (23) Marin-Valencia, I., Roe, C. R., and Pascual, J. M. (2010) Pyruvate carboxylase deficiency: mechanisms, mimics and anaplerosis. *Mol. Genet. Metab.* 101, 9–17.
- (24) Hilpert, W., and Dimroth, P. (1982) Conversion of the chemical energy of methylmalonyl-CoA decarboxylation into a  $Na^+$  gradient. *Nature* 296, 584–585.
- (25) Dimroth, P., Jockel, P., and Schmid, M. (2001) Coupling mechanism of the oxaloacetate decarboxylase  $Na^+$  pump. *Biochim. Biophys. Acta* 1505, 1–14.
- (26) Buckel, W. (2001) Sodium ion-translocating decarboxylases. *Biochim. Biophys. Acta* 1505, 15–27.
- (27) Wood, H. G., Allen, S. H., Stjernholm, R., and Jacobson, B. (1963) Transcarboxylase. III. Purification and properties of methylmalonyl-oxaloacetic transcarboxylase containing tritiated biotin. *J. Biol. Chem.* 238, 547–556.

- (28) Lietzan, A. D., and St. Maurice, M. (2014) Functionally diverse biotin-dependent enzymes with oxaloacetate decarboxylase activity. *Arch. Biochem. Biophys.* 544, 75–86.
- (29) Jitrapakdee, S., St. Maurice, M., Rayment, I., Cleland, W. W., Wallace, J. C., and Attwood, P. V. (2008) Structure, mechanism and regulation of pyruvate carboxylase. *Biochem. J.* 413, 369–387.
- (30) Zeczycki, T. N., St. Maurice, M., and Attwood, P. V. (2010) Inhibitors of pyruvate carboxylase. *Open Enzyme Inhib. J.* 3, 8–26.
- (31) Adina-Zada, A., Zeczycki, T. N., and Attwood, P. V. (2012) Regulation of the structure and activity of pyruvate carboxylase by acetyl CoA. *Arch. Biochem. Biophys.* 519, 118–130.
- (32) Rétey, J., and Lynen, F. (1965) On the biochemical function of biotin. IX. The steric course in the carboxylation of propionyl-CoA. *Biochem. Z.* 342, 256–271.
- (33) Stubbe, J., and Abeles, R. H. (1977) Biotin carboxylations—concerted or not concerted? That is the question! *J. Biol. Chem.* 252, 8338–8340.
- (34) Stubbe, J., Fish, S., and Abeles, R. H. (1980) Are carboxylations involving biotin concerted or nonconcerted? *J. Biol. Chem.* 255, 236–242.
- (35) Yong-Biao, J., Islam, M. N., Sueda, S., and Kondo, H. (2004) Identification of the catalytic residues involved in the carboxyl transfer of pyruvate carboxylase. *Biochemistry* 43, 5912–5920.
- (36) Fry, D. C., Fox, T. L., Lane, M. D., and Mildvan, A. S. (1985) Exchange characteristics of the amide protons of d-biotin and derivatives: implications for the mechanism of biotin enzymes and the role of sulfur in biotin. *J. Am. Chem. Soc.* 107, 7659–7665.
- (37) Attwood, P. V., Tipton, P. A., and Cleland, W. W. (1986) Carbon-13 and deuterium isotope effects on oxalacetate decarboxylation by pyruvate carboxylase. *Biochemistry* 25, 8197–8205.
- (38) O'Keefe, S. J., and Knowles, J. R. (1986) Biotin-dependent carboxylation catalyzed by transcarboxylase is a stepwise process. *Biochemistry* 25, 6077–6084.
- (39) Xiang, S., and Tong, L. (2008) Crystal structures of human and *Staphylococcus aureus* pyruvate carboxylase and molecular insights into the carboxyltransfer reaction. *Nat. Struct. Mol. Biol.* 15, 295–302.
- (40) Attwood, P. V., and Wallace, J. C. (2002) Chemical and catalytic mechanisms of carboxyl transfer reactions in biotin-dependent enzymes. *Acc. Chem. Res.* 35, 113–120.
- (41) Zeczycki, T. N., St. Maurice, M., Jitrapakdee, S., Wallace, J. C., Attwood, P. V., and Cleland, W. W. (2009) Insight into the carboxyl transferase domain mechanism of pyruvate carboxylase from *Rhizobium etli*. *Biochemistry* 48, 4305–4313.
- (42) Lietzan, A. D., and St. Maurice, M. (2013) A substrate-induced biotin binding pocket in the carboxyltransferase domain of pyruvate carboxylase. *J. Biol. Chem.* 288, 19915–19925.
- (43) Yu, L. P., Xiang, S., Lasso, G., Gil, D., Valle, M., and Tong, L. (2009) A symmetrical tetramer for *Staphylococcus aureus* pyruvate carboxylase in complex with coenzyme A. *Structure* 17, 823–832.
- (44) Duangpan, S., Jitrapakdee, S., Adina-Zada, A., Byrne, L., Zeczycki, T. N., St. Maurice, M., Cleland, W. W., Wallace, J. C., and Attwood, P. V. (2010) Probing the catalytic roles of Arg548 and Gln552 in the carboxyl transferase domain of the *Rhizobium etli* pyruvate carboxylase by site-directed mutagenesis. *Biochemistry* 49, 3296–3304.
- (45) St. Maurice, M., Reinhardt, L., Surinya, K. H., Attwood, P. V., Wallace, J. C., Cleland, W. W., and Rayment, I. (2007) Domain architecture of pyruvate carboxylase, a biotin-dependent multifunctional enzyme. *Science* 317, 1076–1079.
- (46) Lietzan, A. D., and St. Maurice, M. (2013) Insights into the carboxyltransferase reaction of pyruvate carboxylase from the structures of bound product and intermediate analogs. *Biochem. Biophys. Res. Commun.* 441, 377–382.
- (47) Studer, R., Dahinden, P., Wang, W. W., Auchli, Y., Li, X. D., and Dimroth, P. (2007) Crystal structure of the carboxyltransferase domain of the oxaloacetate decarboxylase Na<sup>+</sup> pump from *Vibrio cholera*. *J. Mol. Biol.* 367, 547–557.
- (48) Ito, Y., Kondo, H., Shiota, Y., and Yoshizawa, K. (2008) Theoretical analysis of the reaction mechanism of biotin carboxylase. *J. Chem. Theory Comput.* 4, 366–374.
- (49) Warshel, A., and Levitt, M. (1976) Theoretical studies of enzymic reactions: dielectric, electrostatic and steric stabilization of the carbonium ion in the reaction of lysozyme. *J. Mol. Biol.* 103, 227–249.
- (50) Field, M. J., Bash, P. A., and Karplus, M. (1990) A combined quantum mechanical and molecular mechanical potential for molecular dynamics simulations. *J. Comput. Chem.* 11, 700–733.
- (51) Gao, J. L., Ma, S. H., Major, D. T., Nam, K., Pu, J. Z., and Truhlar, D. G. (2006) Mechanisms and free energies of enzymatic reactions. *Chem. Rev.* 106, 3188–3209.
- (52) Senn, H. M., and Thiel, W. (2009) QM/MM methods for biomolecular systems. *Angew. Chem., Int. Ed.* 48, 1198–1229.
- (53) Gómez, H., Polyak, I., Thiel, W., Lluch, J. M., and Masgrau, M. (2012) Retaining glycosyltransferase mechanism studied by QM/MM methods: lipopolysaccharyl- $\alpha$ -1,4-galactosyltransferase C transfers  $\alpha$ -galactose via an oxocarbenium ion-like transition State. *J. Am. Chem. Soc.* 134, 4743–4752.
- (54) Doitomi, K., Kamachi, T., Toraya, T., and Yoshizawa, K. (2012) Inactivation mechanism of glycerol dehydration by diol dehydratase from combined quantum mechanical/molecular mechanical calculations. *Biochemistry* 51, 9202–9210.
- (55) Yan, Q., Han, K. L., and Zhang, C. G. (2013) Fundamental reaction pathway and free energy profile for butyrylcholinesterase-catalyzed hydrolysis of heroin. *Biochemistry* 52, 6467–6479.
- (56) Sheng, X., and Liu, Y. J. (2014) A QM/MM study of the catalytic mechanism of nicotinamidase. *Org. Biomol. Chem.* 12, 1265–1277.
- (57) Shoji, M., Hanaoka, K., Ujiie, Y., Tanaka, W., Kondo, D., Umeda, H., Kamoshida, Y., Kayanuma, M., Kamiya, K., Shirashi, K., Machida, Y., Murakawa, T., and Hayashi, H. (2014) A QM/MM study of the L-threonine formation reaction of threonine synthase: implications into the mechanism of the reaction specificity. *J. Am. Chem. Soc.* 136, 4525–4533.
- (58) Hall, P. R., Zheng, R., Antony, L., Puszta-Carey, M., Carey, P. R., and Yee, V. C. (2004) Transcarboxylase SS structures: assembly and catalytic mechanism of a multienzyme complex subunit. *EMBO J.* 23, 3621–3631.
- (59) Attwood, P. V. (1995) The structure and the mechanism of action of pyruvate carboxylase. *Int. J. Biochem. Cell Biol.* 27, 231–249.
- (60) Olsson, M. H. M., Søndergaard, C. R., Rostkowski, M., and Jensen, J. H. (2011) PROPKA3: consistent treatment of internal and surface residues in empirical pK<sub>a</sub> predictions. *J. Chem. Theory Comput.* 7, 525–537.
- (61) Humphrey, W., Dalke, A., and Schulten, K. (1996) VMD: visual molecular dynamics. *J. Mol. Graphics* 14, 33–38.
- (62) Brooks, B. R., Bruccoleri, R. E., Olafson, B. D., States, D. J., Swaminathan, S., and Karplus, M. (1983) CHARMM: a program for macromolecular energy, minimization, and dynamics calculations. *J. Comput. Chem.* 4, 187–217.
- (63) Brooks, C. L., III, Brunger, A., and Karplus, M. (1985) Active site dynamics in protein molecules: a stochastic boundary molecular dynamics approach. *Biopolymers* 24, 843–865.
- (64) Van Gunsteren, W. F., and Berendsen, H. J. C. (1988) A leap-frog algorithm for stochastic dynamics. *Mol. Simul.* 1, 173–185.
- (65) MacKerell, A. D., Jr., Bashford, D., Bellott, M., Dunbrack, R. L., Jr., Evanseck, J. D., Field, M. J., Fischer, S., Gao, J., Guo, H., Ha, S., Joseph-McCarthy, D., Kuchnir, L., Kuczera, K., Lau, F. T. K., Mattos, C., Michnick, S., Ngo, T., Nguyen, D. T., Prodhom, B., Reiher, W. E., III, Roux, B., Schlenkrich, M., Smith, J. C., Stote, R., Straub, J., Watanabe, M., Wiórkiewicz-Kuczera, J., Yin, D., and Karplus, M. (1998) All-atom empirical potential for molecular modeling and dynamics studies of proteins. *J. Phys. Chem. B* 102, 3586–3616.
- (66) Jorgensen, W. L., Chandrasekhar, J., Madura, J. D., Impey, R. W., and Klein, M. L. (1983) Comparison of simple potential functions for simulating liquid water. *J. Chem. Phys.* 79, 926–935.

- (67) Liang, J. Y., and Lipscomb, W. N. (1990) Binding of substrate CO<sub>2</sub> to the active site of human carbonic anhydrase II: a molecular dynamics study. *Proc. Natl. Acad. Sci. U.S.A.* 87, 3675–3679.
- (68) Pang, Y. P. (2001) Successful molecular dynamics simulation of two zinc complexes bridged by a hydroxide in phosphotriesterase using the cationic dummy atom method. *Proteins* 45, 183–189.
- (69) Karjiban, R. A., Rahman, M. B. A., Basri, M., Salleh, A. B., Jacobs, D., and Wahab, H. A. (2009) Molecular dynamics study of the structure, flexibility and dynamics of thermostable L1 lipase at high temperatures. *Protein J.* 28, 14–23.
- (70) Stote, R. H., and Karplus, M. (1995) Zinc binding in proteins and solution: a simple but accurate nonbonded representation. *Proteins: Struct., Funct., Genet.* 23, 12–31.
- (71) Wu, R. B., Wang, S. L., Zhou, N. J., Cao, Z. X., and Zhang, Y. K. (2010) A proton-shuttle reaction mechanism for histone deacetylase 8 and the catalytic role of metal ions. *J. Am. Chem. Soc.* 132, 9471–9479.
- (72) Dolg, M., Wedig, U., Stoll, H., and Preuss, H. (1987) Energy-adjusted *ab initio* pseudopotentials for the first row transition elements. *J. Chem. Phys.* 86, 866–872.
- (73) Corminboeuf, C., Hu, P., Tuckerman, M. E., and Zhang, Y. K. (2006) Unexpected deacetylation mechanism suggested by a density functional theory QM/MM study of histone-deacetylase-like protein. *J. Am. Chem. Soc.* 128, 4530–4531.
- (74) Sousa, S. F., Fernandes, P. A., and Ramos, M. J. (2007) The carboxylate shift in zinc enzymes: a computational study. *J. Am. Chem. Soc.* 129, 1378–1385.
- (75) Wu, R. B., Hu, P., Wang, S. L., Cao, Z. X., and Zhang, Y. K. (2010) A flexibility of catalytic zinc coordination in thermolysin and HDAC8: a Born–Oppenheimer *ab initio* QM/MM molecular dynamics study. *J. Chem. Theory Comput.* 6, 337–343.
- (76) Field, M. J., Bash, P. A., and Karplus, M. (1990) A combined quantum mechanical and molecular mechanical potential for molecular dynamics simulations. *J. Comput. Chem.* 11, 700–733.
- (77) de Vries, A. H., Sherwood, P., Collins, S. J., Rigby, A. M., Rigoletto, M., and Kramer, G. J. (1999) Zeolite structure and reactivity by combined quantum-chemical–classical calculations. *J. Phys. Chem. B* 103, 6133–6141.
- (78) Bakowies, D., and Thiel, W. (1996) Hybrid models for combined quantum mechanical and molecular mechanical approaches. *J. Phys. Chem.* 100, 10580–10594.
- (79) Ruiz-Lopez, M. F. (2003) Combined QM/MM calculations in chemistry and biochemistry. *J. Mol. Struct.: THEOCHEM* 632, ix.
- (80) Ahlrichs, R., Bär, M., Häser, M., Horn, H., and Kölmel, C. (1989) Electronic structure calculations on workstation computers: the program system turbomole. *Chem. Phys. Lett.* 162, 165–169.
- (81) Smith, W., and Forester, T. R. (1996) ChemShell—a modular software package for QM/MM simulation. *J. Mol. Graphics Modell.* 14, 136–141.
- (82) Billeter, S. R., Turner, A. J., and Thiel, W. (2000) Linear scaling geometry optimization and transition state search in hybrid delocalised internal coordinates. *Phys. Chem. Chem. Phys.* 2, 2177–2186.
- (83) Nocedal, J. (1980) Updating quasi-Newton matrices with limited storage. *Math. Comput.* 35, 773–782.
- (84) Liu, D. C., and Nocedal, J. (1989) On the limited memory BFGS method for large scale optimization. *Math. Prog.* 45, 503–528.
- (85) Banerjee, A., Adams, N., Simons, J., and Shepard, R. (1985) Search for stationary points on surfaces. *J. Phys. Chem.* 89, 52–57.
- (86) Sherwood, P., de Vries, A. H., Guest, M. F., Schreckenbach, G., Catlow, C. R. A., French, S. A., Sokol, A. A., Bromley, S. T., Thiel, W., Turner, A. J., Billeter, S., Terstegen, F., Thiel, S., Kendrick, J., Rogers, S. C., Casci, J., Watson, M., King, F., Karlsen, E., Sjøvoll, M., Fahmi, A., Schafer, A., and Lennartz, C. (2003) QUASI: a general purpose implementation of the QM/MM approach and its application to problems in catalysis. *J. Mol. Struct.: THEOCHEM* 632, 1–28.
- (87) Granjon, T., Maniti, O., Auchli, Y., Dahinden, P., Buchet, R., Marcillat, O., and Dimroth, P. (2010) Structure–function relations in oxaloacetate decarboxylase complex. Fluorescence and infrared approaches to monitor oxomalonate and Na<sup>+</sup> binding effect. *PLoS One* 5, e10935.
- (88) Goodall, G. J., Baldwin, G. S., Wallace, J. C., and Keech, D. B. (1981) Factors that influence the translocation of the N-carboxybiotin moiety between the two sub-sites of pyruvate carboxylase. *Biochem. J.* 199, 603–609.
- (89) Attwood, P. V., Wallace, J. C., and Keech, D. B. (1984) The carboxybiotin complex of pyruvate carboxylase. A kinetic analysis of the effects of Mg<sup>2+</sup> ions on its stability and on its reaction with pyruvate. *Biochem. J.* 219, 243–251.
- (90) Thorpe, I. F., and Brooks, C. L., III (2005) Conformational substates modulate hydride transfer in dihydrofolate reductase. *J. Am. Chem. Soc.* 127, 12997–13006.
- (91) Klähn, M., Braun-Sand, S., Rosta, E., and Warshel, A. (2005) On possible pitfalls in *ab initio* quantum mechanics/molecular mechanics minimization approaches for studies of enzymatic reactions. *J. Phys. Chem. B* 109, 15645–15650.
- (92) Hu, P., and Zhang, Y. K. (2006) Catalytic mechanism and product specificity of the histone lysine methyltransferase SET7/9: an *ab initio* QM/MM-FE study with multiple initial structures. *J. Am. Chem. Soc.* 128, 1272–1278.
- (93) Parkin, G. (2004) Synthetic analogues relevant to the structure and function of zinc enzymes. *Chem. Rev.* 104, 699–767.
- (94) Fung, C. H., Mildvan, A. S., Allerhand, A., Komoroski, R., and Scrutton, M. C. (1973) Interaction of pyruvate with pyruvate carboxylase and pyruvate kinase as studied by paramagnetic effects on <sup>13</sup>C relaxation rates. *Biochemistry* 12, 620–629.
- (95) Fung, C. H., Mildvan, A. S., and Leigh, J. S., Jr. (1974) Electron and nuclear magnetic resonance studies of the interaction of pyruvate with transcarboxylase. *Biochemistry* 13, 1160–1169.
- (96) Attwood, P. V., and Cleland, W. W. (1986) Decarboxylation of oxaloacetate by pyruvate carboxylase. *Biochemistry* 25, 8191–8196.
- (97) Ganguly, A., Bevilacqua, P. C., and Hammes-Schiffer, S. (2011) Quantum mechanical/molecular mechanical study of the HDV ribozyme: impact of the catalytic metal ion on the mechanism. *J. Phys. Chem. Lett.* 2, 2906–2911.
- (98) Polyak, I., Reetz, M. T., and Thiel, W. (2012) Quantum mechanical/molecular mechanical study on the mechanism of the enzymatic Baeyer–Villiger reaction. *J. Am. Chem. Soc.* 134, 2732–2741.
- (99) Lonsdale, R., Houghton, K. T., Åzurek, J., Bathelt, C. M., Foloppe, N., de Groot, M. J., Harvey, J. N., and Mulholland, A. J. (2013) Quantum mechanics/molecular mechanics modeling of regioselectivity of drug metabolism in cytochrome P450 2C9. *J. Am. Chem. Soc.* 135, 8001–8015.
- (100) Elsässer, B., Fels, G., and Weare, J. H. (2014) QM/MM simulation (B3LYP) of the RNase A cleavage-transesterification reaction supports a triester A(N) + D(N) associative mechanism with an O2' H internal proton transfer. *J. Am. Chem. Soc.* 136, 927–936.
- (101) Ahmad, F., Lygre, D. G., Jacobson, B. E., and Wood, H. G. (1972) Transcarboxylase. XII. Identification of the metal-containing subunits of transcarboxylase and stability of the binding. *J. Biol. Chem.* 247, 6299–6305.
- (102) Carver, J. A., Baldwin, G. S., Keech, D. B., Bais, R., and Wallace, J. C. (1988) Inactivation of chicken liver pyruvate carboxylase by 1,10-phenanthroline. *Biochem. J.* 252, 501–507.
- (103) Dimroth, P., and Thomer, A. (1992) The sodium ion pumping oxaloacetate decarboxylase of *Klebsiella pneumoniae*. Metal ion content, inhibitors and proteolytic degradation studies. *FEBS Lett.* 300, 67–70.